UNIVERSTIY OF CALIFORNIA, SAN DIEGO

Evaluation of Porous Silicon - Perfluorinated Polymer Composite Sensors and Optimization of Porous Silicon Microparticle Synthesis

A Thesis submitted in partial satisfaction of the requirements for the degree Master of Science

in

Chemistry

by

Rhiannon Marie Kennard

Committee in charge:

Professor Michael J. Sailor, Chair
Professor Francesco Paesani
Professor Jeffrey Rinehart

2016

The Thesis of Rhiannon Marie Kennard is approved, and is acceptable in quality and form for publication on microfilm and electronically:

Chair

University of California, San Diego

2016

DEDICATION

To my family

TABLE OF CONTENTS

LIST OF FIGURES

ACKNOWLEDGMENTS

First I would like to thank Professor Michael Sailor. Professor Sailor has been an excellent mentor, both in my undergraduate and Masters careers. He gave me the opportunity to work on highly interesting and impactful projects as an undergraduate, and pushed me to come up with my own ideas for projects, which I have come to realize are rare qualities in an undergraduate mentor. He also taught me vital skills for my future career, in experiment planning and analysis as well as in proposal writing. He has provided valuable career advice and guidance, and has helped greatly with the PhD application process and a variety of scholarship applications. This year Professor Sailor gave me the unusual opportunity to do full time research for the better part of the year as a Master's student. The experience was invaluable preparation for my PhD. Professor Sailor has been an inspiration for me to pursue a career in science, and to be a good mentor to others.

I would next like to thank the members of the Sailor group. Thank you for all your guidance, and for being pleasant and fun co-workers. I particularly appreciate the feedback that you have given me for posters and presentations, and for my thesis defense talk. Tushar and Joanna, thank you for all the help and advice regarding planning experiments, data analysis, and equipment. Dokyoung, thank you for everything I have learned from you regarding proposal writing. B.J., thank you for the advice regarding thesis defenses. Emily Anglin, thank you for teaching me many good research habits; I used them for the experiments in this thesis. Andrea, Jessica, and Nicole, thank you for being excellent lab managers. Your work has made my work much easier. And Andrea, thank you for going with me so many times to the SEM.

To all my friends in the Sailor group, thank you for the fun times we have had together. I have had so much fun seeing you every day for lunch and sometimes coffee, eating delicious food in Convoy, going to Karaoke, and occasionally going to exciting places like Irvine or Universal Studios. I will miss you, and I appreciate the encouragement and support you that have shown me.

To my close friends Ilya and Jason, thank you for all the good times these past five years. There are things I would not have been able to achieve without your support and patience. I will miss these years of sitting in Jason's room with BBQ watching hilarious shows and trying to out-pun each other.

And last but not least, to my family, Adrienne, Mark, Alanna, Joanie, Paul, Ann, Jim, Carol, Larry, Karen, and Marcos. Thank you for being loving and supportive, and for giving me the tools I needed to succeed. These past five years, hearing your voices on the phone has many times been the highlight of my day.

Chapter 1, in full, is being prepared for submission for publication of the material. Kennard, Rhiannon; Wang, Joanna; Lee, Gha Y.; Bisiewicz, Rachel H.; Cortez Lemus, Norma A.; Cao, Xiaoyu C.; Anglin, Emily J.; Park, Jennifer S.; Potocny, Andrea; Bernhard, Drew; Li, Jianlin; Sailor, Michael J. The thesis author was the primary investigator and author of this material.

Chapter 2, in full, is being prepared for submission for publication of the material. Kennard, Rhiannon; Sailor, Michael J. The thesis author was the primary investigator and author of this material.

ABSTRACT OF THE THESIS

Evaluation of Porous Silicon - Perfluorinated Polymer Composite Sensors and Optimization of Porous Silicon Microparticle Synthesis

by

Rhiannon Marie Kennard

Master of Science in Chemistry

University of California, San Diego 2016

Professor Michael J. Sailor, Chair

Porous silicon photonic crystal-poly(vinylidiene fluoride) polymer composites were synthesized to fabricate a sensor exhibiting tunable hydrophobicity and stability in basic conditions. Poly(vinylidiene fluoride) polymer was infiltrated into porous silicon

photonic crystals via the melt-cast method. Partial removal of the hydrophilic silicon template enabled tuning of the hydrophobicity of the silicon-polymer composites over a water contact angle range of 60°-110°. The composites exhibited much greater stability at pH 12 than did the free-standing porous silicon templates. The mechanism of dissolution of the silicon template was examined. In a separate study, perforated etching of silicon wafers was assessed for high-yield preparation of porous Si microparticles, with a focus on optimizing ultrasonication conditions. The effects of increasing the amount of cavitation on particle size and size distribution were assessed. Concentration of films during ultrasonication and duration of ultrasonication on particle were systematically investigated for efficient synthesis of ~70μm particles. The effects of pre-treatment by mechanical crushing on nucleation uniformity, on yield, and yield reproducibility were also assessed.

CHAPTER ONE.

EVALUATION OF POROUS SILICON – PERFLUORINATED POLYMER COMPOSITE SENSORS

1.1 Introduction

Porous silicon (pSi) photonic crystals are attractive materials for sensing applications due to their low cost [1] and to the ease with which the material can be functionalized. [1, 2, 3, 4, 5] pSi nanostructures also exhibit very high available surface area for analyte adsorption (up to a few m^2/cm^3), [3] and thus have very high sensitivity. PSi is an attractive template for polymer infiltration due to the wide variety of pSi nanostructures that can be fabricated, each with highly tunable porosity and thickness. [6, 7, 8, 9, 10]

Rugate pSi nanostructures are useful for vapor or volatile organic compound (VOC) sensing applications because they provide a simple, sensitive and inexpensive means to detect the analyte. [1, 2, 11, 12, 13, 14, 15] A pSi rugate filter is a one-dimensional structure consisting of alternating layers of low and high porosity, such that the pore wall has a sinusoidal shape. [6] Light reflected off this surface constructively interferes, giving the surface a bright color in the visible range of the spectrum. Infiltration of materials with different refractive indices causes the photonic stop band to reversibly shift, enabling detection of a variety of analytes. [1, 2, 11, 12, 13, 14, 15]

Sensitive detection of vapors or volatile organic compounds (VOCs) typically involves tailoring the surface chemistry of the pSi layer to the specific analyte. [3, 13] Salonen and co-workers found that acetylene-carbonized pSi sensors exhibited different sensitivity to water vapor, with sensors carbonized at higher temperatures exhibiting greater hydrophilicity. [13] Ruminski and co-workers found that heptane was more sensitively detected using a low-temperature acetylene-carbonized porous silicon surface, whereas a more hydrophilic oxidized surface yielded better detection of isopropyl alcohol.[3] While

these methods are simple and efficient, different functionalization methods are still required to sensitively detect analytes with different hydrophobicities.

Successful fabrication of pSi gas sensors also involves stabilizing the surface of porous silicon, because freshly-prepared porous silicon is unstable in aqueous or environmental conditions. [9, 14, 15] Carbon coatings provide an attractive solution to this issue, as they create a physical barrier between the unstable pSi surface and the environment. Salonen and co-workers were able to reversibly detect amine compounds using carbonized pSi sensors, which is remarkable given that basic compounds are known to degrade pSi. [15] An alternate approach involves fabricating polymer replicas of porous silicon photonic crystals. [10] Replicas are typically made by melting a polymer into the pSi structure (the "melt-cast" method), or by polymerizing a precursor in the pSi structure. The silicon template is then dissolved, leaving a polymer with a structure complementary to that of the template. This approach circumvents the stability issues surrounding pSi sensors, as many polymers are much more durable in aqueous or environmental conditions than porous silicon, exhibit affinity towards volatile organic analytes, and provide greater mechanical stability and flexibility than pSi sensors. [8, 10, 11] In previous studies, poly(furfuryl alcohol) replicas of porous silicon rugate filters successfully detected toluene, methanol, hexanes, and ethanol. [11]

In this work, we present a pSi-polymer composite sensor exhibiting tunable hydrophobicity. We used the melt-cast method [8] to infiltrate poly(vinylidiene fluoride) into a porous silicon rugate filter and tuned sensor hydrophobicity by slowly dissolving the porous silicon template, thereby increasing the fraction of hydrophobic polymer in the sensing layer. The sensor exhibited much greater stability at high pH than did the control

porous silicon template, and was also much more mechanically robust. We anticipate that this work will provide a simple method to tune the hydrophobicity of polymer replica sensors to increase sensitive detection of a variety of analytes.

1.2 Experimental Section

1.2.1 Materials

Poly(vinylidiene fluoride) (analytical standard for GPC, with average 180,000g/mol M_w) beads were purchased from Sigma-Aldrich Chemicals. Silicon wafers, highly boron-doped (resistivity < 0.0015 Ω-cm), polished on the (100) face, 525 ± 25 μm thick were purchased from Virginia Semiconductors.

1.2.2 Fabrication of Porous Silicon Templates

Porous silicon rugate photonic crystals were electrochemically etched using a 3:1 (v:v) solution of 48% aqueous hydrofluoric acid:ethanol electrolyte (CAUTION: HF is highly toxic and proper care should be exerted to avoid contact with skin or lungs), platinum counter electrode, and a sinusoidal current density-time waveform of 25-100 mA/cm^2 for 240 repeats and a ~5s period. The porous films were lifted off the substrate using a current density of 10 mA/cm^2 for 300 s in a 1:15 (v:v) solution of 48% aqueous hydrofluoric acid and ethanol electrolyte. Scanning electron microscopy (SEM) images indicated that the freestanding films were approximately 42μm thick, and from that the porosity was calculated to be 53% porosity using the SLIM method (with ethanol as the filling liquid).[9] Samples were then thermally oxidized at 500°C for three hours in air in a tube furnace. The thickness of the oxidized films measured by SEM was 46μm, and from that the porosity was calculated to be 43% using the SLIM method (with ethanol as the filling liquid) and a layer refractive index of 2.[9]

1.2.3 Fabrication of Porous Silicon - Poly(vinylidiene fluoride) Photonic Crystals

Composite photonic crystals were synthesized using the melt-cast method.[8] Poly(vinylidiene fluoride) beads were melted into disks of ~1cm diameter for ease of use.

The disks were then placed on top of a freestanding pSi film. The poly(vinylidiene fluoride) and pSi assembly was placed on a hot plate at 240°C for 1.25 hours to allow the polymer to infiltrate. The pSi template was slowly removed by dissolution in a 0.05M potassium hydroxide solution (10% ethanol in water). [9] Ethanol was added to the KOH solution to improve wettability of the composite and enhance reproducibility of the dissolution. All characterization (infrared spectroscopy, optical characterization, electron microscopy, contact angle) was performed on the side of the film opposite to the side on which the PVDF was placed.

1.2.4 Infrared Spectroscopy

Selective dissolution of the silicon template from the pSi-PVDF composites was determined by attenuated total reflectance (ATR) Fourier transform-infrared (FTIR) spectroscopy using a Thermo Scientific Nicolet 6700 FTIR spectrometer fitted with a Smart iTR sampling accessory. Spectra were acquired from 650 to 4000 cm^{-1}, with an average of 128 scans and a resolution of 4 cm^{-1}.

1.2.5 Optical Reflectance and Transmission Characterization

Reflectance spectra were acquired using a CCD spectrometer (Ocean Optics USB-4000), a tungsten white light source (Ocean Optics LS-1), and a bifurcated fiber optic cable as described previously. [9] One branch of the optical fiber was connected to the light source, and the other end to the spectrometer. The branch of the fiber optic cable containing both incoming and outgoing light was attached to a microscope objective lens to acquire reflectance spectra perpendicular to the sample surface, with a spot size of ~1mm^2. A Hydrogen-Deuterium light source (Ocean Optics DH-2000) and photomultiplier-tube spectrometer (Ocean Optics QE65 Pro) were used for composites with stop bands below

460nm. Ocean Optics Spectra Suite software was used to acquire all spectra. Reflectance spectra were taken in air, and also after dropping ethanol onto the samples. Average porosity was obtained using the SLIM method (with ethanol as the filling liquid). [9]

Theoretical stopband position after PVDF infiltration was calculated using a two-component Looyenga model, as previously described. [9] The average porosity of the oxidized pSi template was calculated from SLIM to be 0.43 (43%), the oxidized pSi skeleton index was assumed to be 2 and the PVDF refractive index was assumed to be 1.42. The oxidized pSi skeleton index was calculated from the film thickness and from the stopbands of the oxidized pSi in air and ethanol. The special periodicity d_p of the layers in the nanostructure was calculated by dividing the total thickness (46,000nm) by the number of repeats (240), to obtain d_p = 191nm. From these values, the theoretical stopband wavelength λ_{SB}, assuming 100% PVDF infiltration, was calculated from the $\lambda_{SB} = 2n_{avg}d_p$, where n_{avg} is the average refractive index of the composite, calculated to be 1.45. [9] The percent PVDF infiltration was calculated as $100(\Delta\lambda_{obs}/\Delta\lambda_{calc})$, where $\Delta\lambda_{obs}$ is the observed stopband shift and $\Delta\lambda_{calc}$ is the calculated stopband shift.

Transmission spectra were acquired using a CCD spectrometer (Ocean Optics USB-4000), a tungsten white light source (Ocean Optics LS-1), and two non-bifurcated fiber optic cables. One fiber optic cable connected the light source to a lens which focused the light to a spot size of ~1mm^2 on the sample. The sample was held on a transparent microscope slide. The second fiber optic cable was connected to the opposite side of the sample so as to transfer the transmitted light to the spectrometer. A collimator was attached to the second fiber optic to ensure that all transmitted light was collected. Ocean Optics Spectra Suite software was used to acquire all spectra.

1.2.6 Scanning Electron Microscopy (SEM)

Films were imaged using a Scanning Electron Microscope (SEM - FEI XL30 with accelerating voltage of 7kV and spot size of 3nm). Energy dispersive X-ray (EDX) analysis was performed on the same instrument, with an accelerating voltage of 20kV and a spot size of 4nm. The samples were first sputter-coated with iridium (Emitech K575X Sputter Coater).

1.2.7 Contact Angle

Hydrophobicity of the pSi-PVDF composites was characterized by water contact angle with the sample surface using a Theta Optical Tensiometer (KSV, Finland), averaging values from five different samples.

1.3 Results and Discussion

1.3.1 Preparation of the pSi Template and of the pSi-PVDF Composites

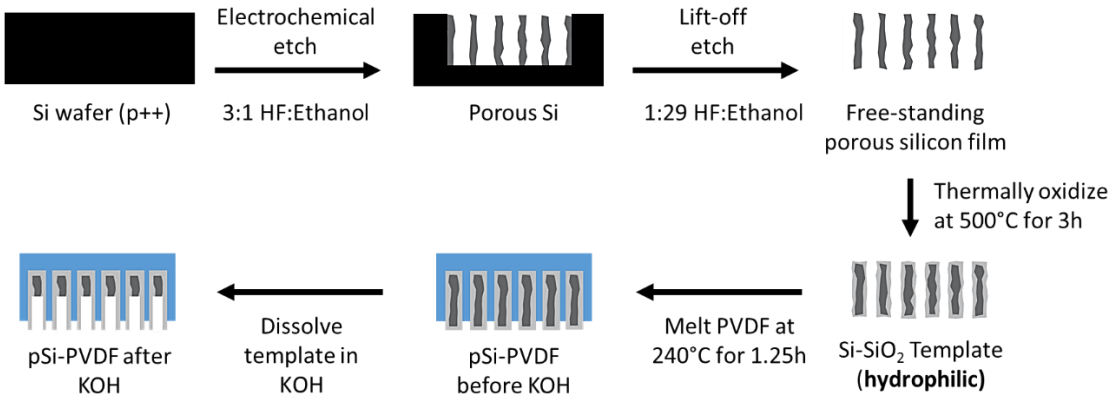

Figure 1.1. Procedure used to fabricate porous silicon rugate filters and infiltrate PVDF into the oxidized pSi templates (adapted from figure made by Joanna Wang and from reference 9).

The strategy for the preparation of porous silicon-poly(vinylidiene fluoride) composites (pSi-PVDF) is outlined in Figure 1.1. Briefly, PVDF disks were melted into oxidized porous silicon rugate filter templates, and the templates were slowly removed via dissolution in 0.05M KOH (see Fig. A.1.1)

1.3.2 Probing the Open Porosity and Sensing Capabilities of the pSi-PVDF Composites

The pSi templates displayed open pores (Fig. 1.2.a). As the PVDF polymer infiltrated the silicon template, the pores closed (Fig. 1.2.a). EDX analysis confirmed that the imaged area contained silicon, thus that the imaged area was the pSi-PVDF composite (Fig. A.1.2.). Open pores were observed after 2h of soaking in KOH, suggesting removal of the pSi template. Selective removal of the pSi template was confirmed by Fourier Transform Infrared Spectroscopy (Fig. 1.4) and by EDX (Fig. A.1.3).

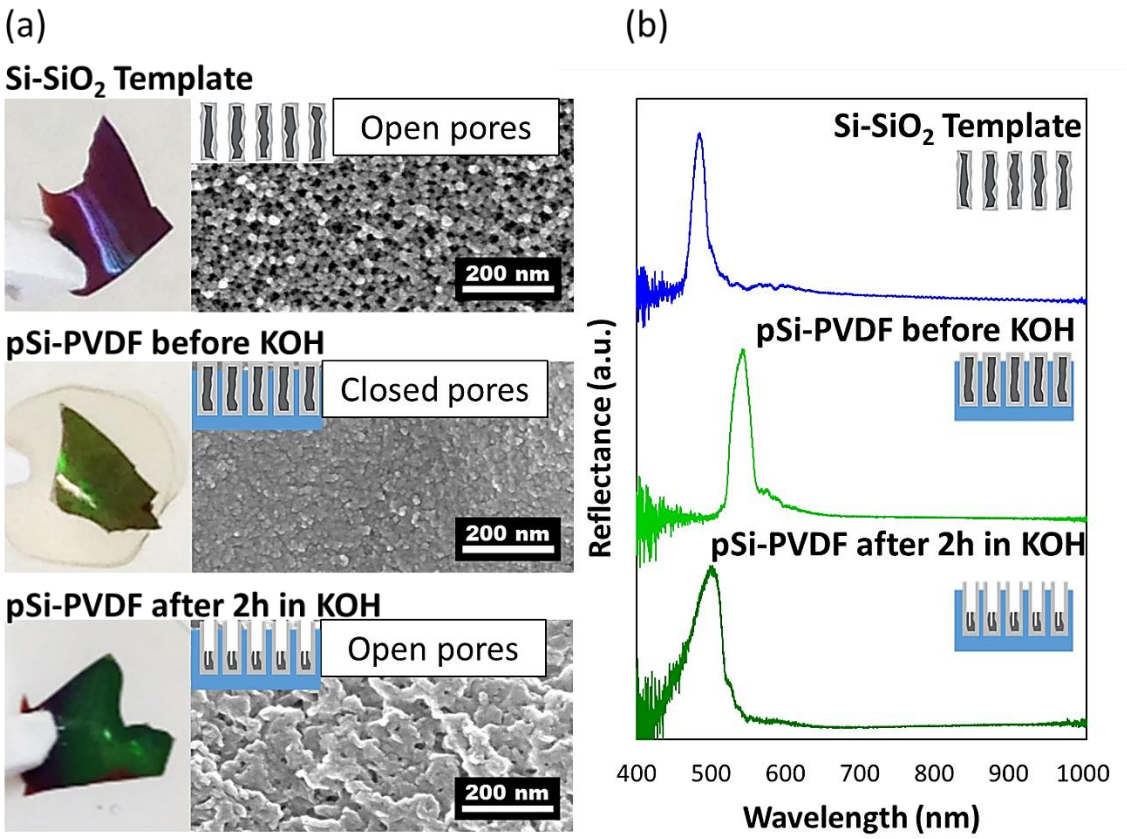

Figure 1.2. (a) Top view SEM images and pictures and (b) reflectance spectra in air of the oxidized pSi template, of the pSi-PVDF composite pre-dissolution, and of the pSi-PVDF composite after 2h of dissolution in KOH. Pictures in (a) were taken with an iPhone 5c.

Optical reflectance characterization also indicated successful infiltration of PVDF into the template and removal of pSi (Fig. 1.2). The pSi template and pSi-PVDF composites displayed reflectance spectra characteristic of the rugate structure (Fig. 1.2.b). As PVDF infiltrated the pSi template, the refractive index of the material in the pores of the template increased from 1.0 (air) to 1.4 (PVDF). The rugate stop band correspondingly red-shifted from 482nm (template) to 532nm (composite) upon PVDF infiltration (Fig. 1.2.b). The theoretical stopband was calculated to shift to 554nm. The observed 50nm stopband shift was lower than the theoretical stopband shift, 72nm, indicating ~70% PVDF infiltration. Yet, the pores of the composite before dissolution appeared completely filled (Fig. 1.2.a)

and the reflectance spectrum of the composite before dissolution showed only one narrow rugate peak, suggesting that the PVDF infiltrated the full thickness of the pSi template (Fig. 1.2.b). SEM and EDX analysis confirmed full infiltration (Figs. 1.3.a and 1.3.b). We therefore attribute the ~70% PVDF infiltration to PVDF successfully infiltrating the mesopores of the template, but not the micropores. This interpretation is consistent with the results of a current polymer infiltration study, which indicate that larger molecular weight polymers preferentially infiltrate the mesopores instead of the micropores of pSi; our polymer molecular weight is indeed elevated (180,000g/mol – manuscript in preparation). The slight difference in peak shape between the template and the composite before KOH and the non-uniformity in these peaks can be attributed to non-uniformity in the etching procedure (Fig. 1.2.b).

Soaking the composite in KOH resulted in pore opening (Fig. 1.2.a) and thus in air (refractive index of 1.0) being introduced into the composite. The overall refractive index of the composite thus decreased, and correspondingly, the rugate stop band blue-shifted (Fig. 1.2.b). The reflectance spectrum of the composite after dissolution showed peak broadening compared to that of the composite before dissolution (Fig. 1.2.b). We attribute this broadening to uneven dissolution of the silicon template (Fig. 1.3.c). Cross-sectional images of the pSi-PVDF composite after 2h in KOH showed large open pores close to the surface of the composite, and much smaller pores further in the composite (Fig. 1.3.c). We concluded that the aqueous KOH solution dissolved the pSi-SiO_2 closest to the surface of the composite before dissolving the pSi-SiO_2 located further in the composite. This would give rise to multiple superimposed rugate structures, corresponding to the larger-pore and smaller-pore layers. The reflectance spectrum of this structure should show multiple peaks;

however, if the peaks are sufficiently close together, they may appear as one broad peak, such as the peak of the composite after 2h in KOH (Fig. 1.2.b). No significant peak broadening was observed before and after infiltration (Fig. 1.2.b), indicating that the PVDF infiltrated the full length of the silicon template. This was also confirmed by SEM and EDX (Fig. 1.3.b).

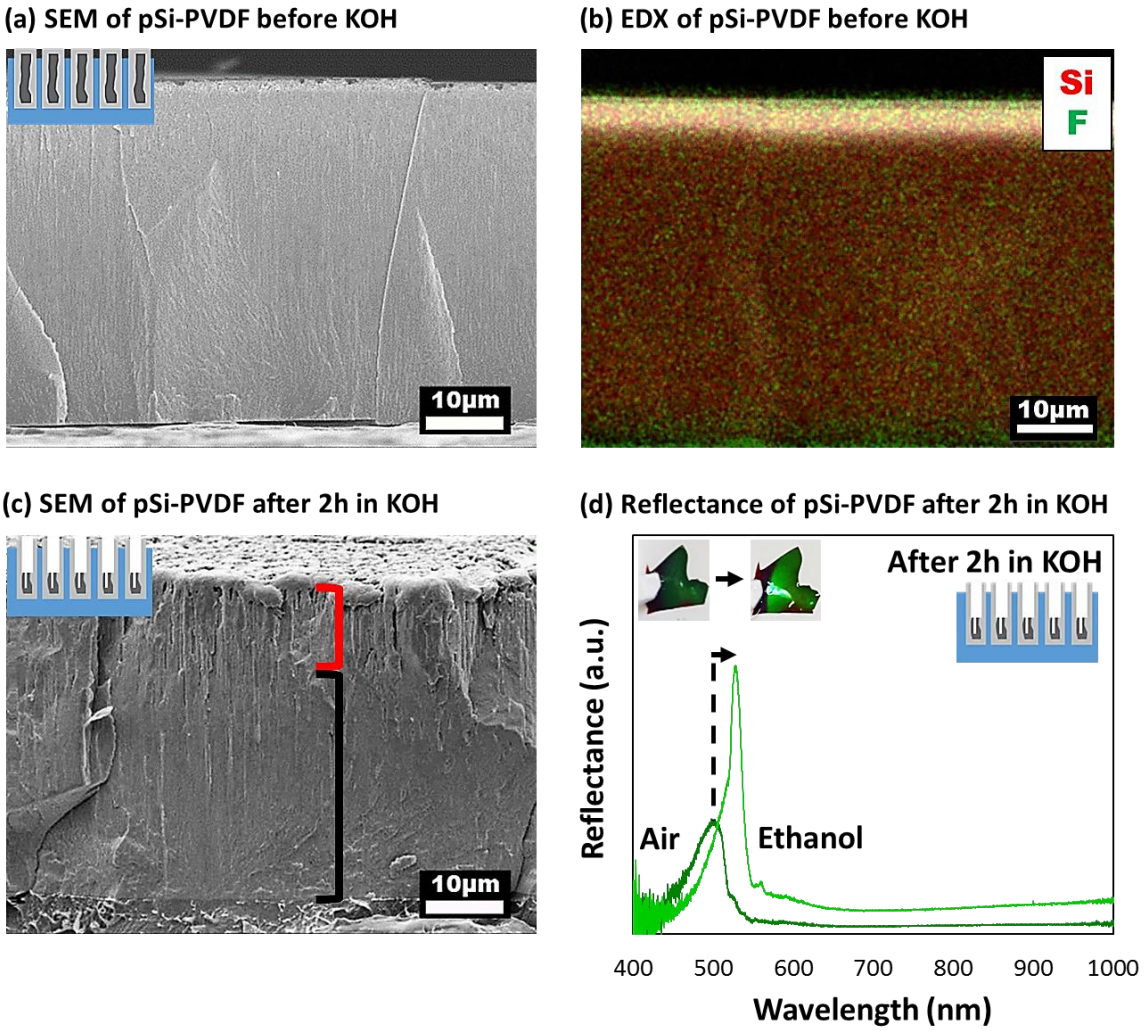

Figure 1.3. (a) Cross-sectional SEM and (b) EDX image of the pSi-PVDF composite before dissolution, (c) Cross-sectional SEM and (d) Reflectance spectra and pictures in air and ethanol of a composite after 2h dissolution in KOH. The red bracket in (c) refers to the larger-pore layer and the black bracket to the smaller-pore layer.

After 2h dissolution in KOH, the composites displayed a stopband shift of ~22nm, from 508nm in air to 530nm in ethanol, demonstrating the composite's sensing capabilities (Fig. 1.3.d). The reflectance peak in air was significantly broader than the peak in ethanol (Fig. 1.3.d), consistent with formation of multiple superimposed rugate structures during the dissolution process. The higher porosity layers would exhibit a greater peak shift than the lower porosity layers, giving rise to peak superposition when the compo-site is soaked in ethanol, and thus to a much sharper peak. This interpretation also explains the asymmetry observed in both the air and ethanol peaks.

1.3.3 Chemical Dissolution of the Si-SiO_2 Template

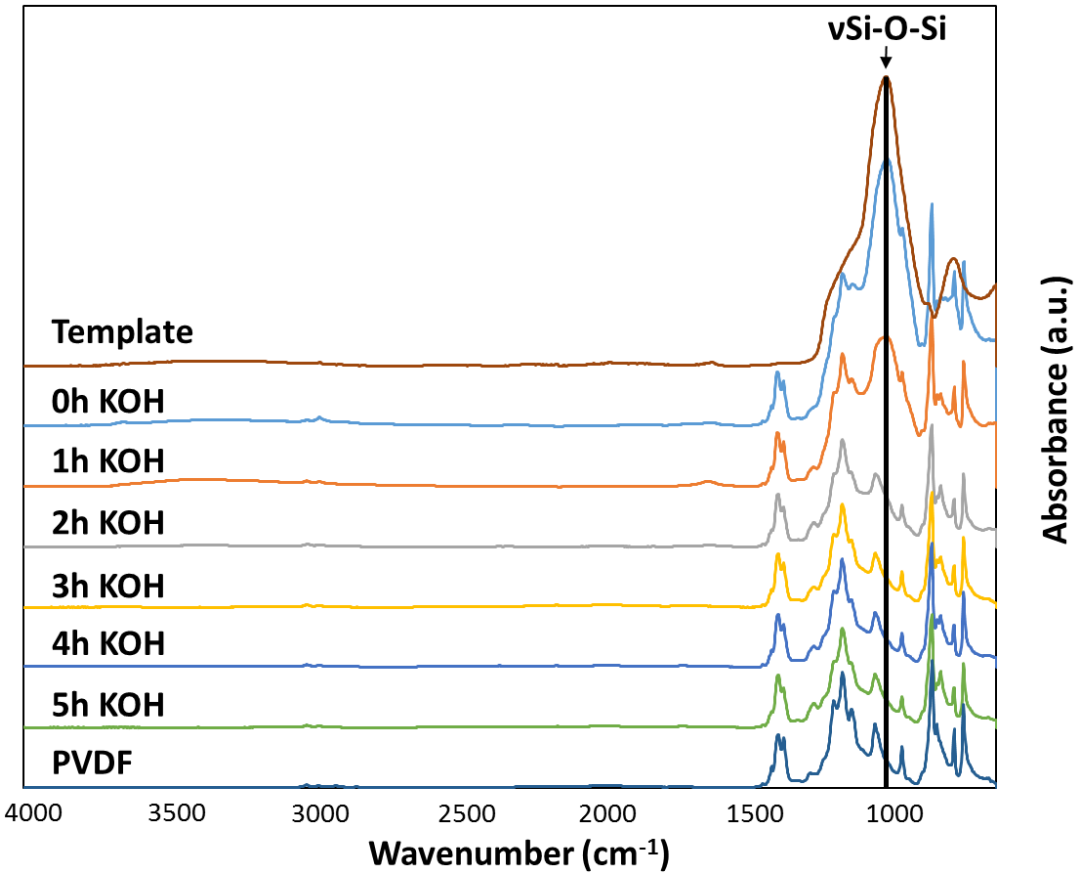

Figure 1.4. Fourier-Transform Infrared (FTIR) spectra of the oxidized porous silicon template, the pSi-PVDF composite before dissolution in KOH, the composite after 1, 2, 3, 4, and 5h of dissolution in KOH, and an unmodified PVDF bead.

The porous silicon templates contained an outer layer of SiO_2, whose characteristic vibrational modes were confirmed in the FTIR spectrum: v(Si-O_2) stretching vibrations at 1030cm^{-1} and 1214cm^{-1} (Fig. 1.4). [9] The pSi-PVDF composites contained both the SiO_2 stretches and the characteristic PVDF vibrations, indicating infiltration of the PVDF into the template: v(C-F_2) bending at 762cm^{-1}, v(C-H_2) rocking at 795cm^{-1}, v(C-H_2) rocking at 870cm^{-1}, v(C-H_2) twist deformation at 976cm^{-1}, v(C-F_2) symmetrical stretching at 1062cm^{-1}, v(C-F_2) symmetrical stretching vibrations at 1143cm^{-1} and 1173cm^{-1}, v(C-F_2) asymmetrical stretching vibration at 1203cm^{-1}, v(C-H_2) bending or scissoring vibrations at ~1394-1450cm^{-1}, and v(C-H_3) symmetric and asymmetric stretching vibrations at 2990cm^{-1} and 3029cm^{-1} (Fig. 1.4). [9, 16, 17, 18] The intensity of the SiO_2 stretch decreased with increasing dissolution time in KOH but the intensity of the PVDF peaks did not change, indicating selective removal of the pSi template.

1.3.4 Fabrication of a Sensor with Tunable Hydrophobicity

The pSi template was slowly dissolved from the composite in a solution of dilute potassium hydroxide (Fig. 1.1). [9] The contact angle of water on the composite was measured as the pSi template dissolved (Fig. 1.5). Before dissolution, the contact angle was ~60°, indicating that the composite was hydrophilic. This was higher than the contact angle of the template (~14°), presumably due to the presence of PVDF in the composite. With gradual removal of the hydrophilic template, the contact angle increased to ~110°. This is greater than the measured contact angle of pure PVDF (~89°), possibly because the layer exhibited Cassie behavior. [14] The Cassie and Baxter relationship predicts that the apparent contact angle of water on a rough or porous surface with low surface energy increases with decreasing solid surface fraction or increasing air surface fraction. [19] The elevated contact

angles observed after 3h of dissolution indicate that the silicon remaining in the composite was sufficiently buried that the water drop did not interact with it (Fig. 1.5). The contact was highly tunable between 60° and 110° (Fig. 1.5), indicating that the 3h dissolution process was slow enough to have good control over hydrophobicity, yet was fast enough to be practical.

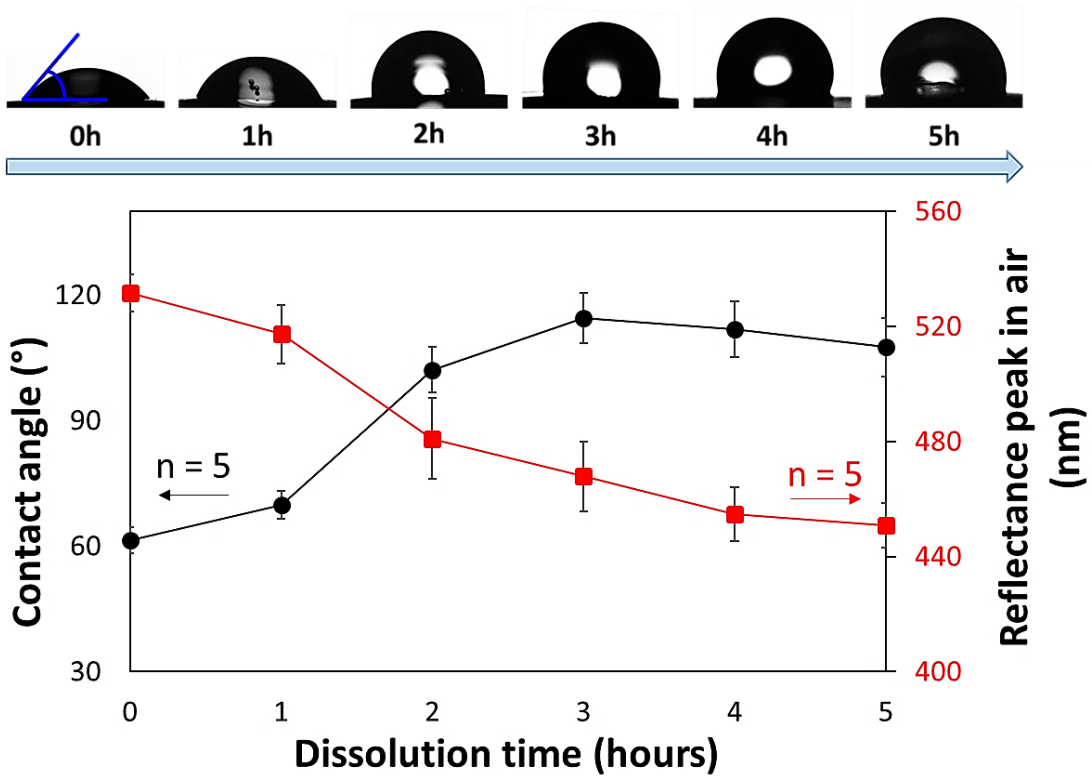

Figure 1.5. Contact angle of water on the composites (black) and reflectance stop band peak of the composites in air (red) after 0, 1, 2, 3, 4 and 5h of soaking in KOH. All data points represent the average of 5 composites.

The increase in contact angle from 60° (pre-dissolution) to 110° (3h dissolution) correlated with a decrease in the reflectance peak in air of the composites (Fig. 1.5); consistent with the interpretation that the peak should blue-shift as more pSi dissolves and thus as more air enters the sample. This blue-shift also correlated with the decrease of the SiO_2 peak intensities in FTIR (Fig. 1.4).

1.3.5 Stability of the pSi-PVDF Composites

The stability of the pSi-PVDF composites in 0.05M KOH (10% ethanol) was compared with that of the pSi template alone (Fig. 1.6) by examining the percent transmission of the samples as they soaked in KOH. Silicon absorbs strongly at low wavelengths (Fig. 1.6.a), and correspondingly the pSi template and the pSi-PVDF composite before dissolution exhibited ~0% transmission (Fig. 1.6.a).[9] Removal of silicon was monitored by tracking the transmission of the samples at 550nm (Fig. 1.6.b). PVDF is colorless (Fig. 1.6.a), so any changes in transmission were assumed to be due to silicon removal.

The pSi-PVDF composites displayed very low transmission at 550nm after 4h in KOH indicating that large amounts of crystalline silicon remained in the sample. EDX analysis confirmed the presence of silicon in the composites after 6h in KOH (Fig. A.1.3). The pSi template, however, exhibited elevated transmission after 2h, and full dissolution after 3h (Fig. 1.6.b). The pSi-PVDF composites were thus much more stable than the pSi templates. The pSi-PVDF composites also exhibited much greater mechanical stability than did the pSi templates (Fig. A.1.4).

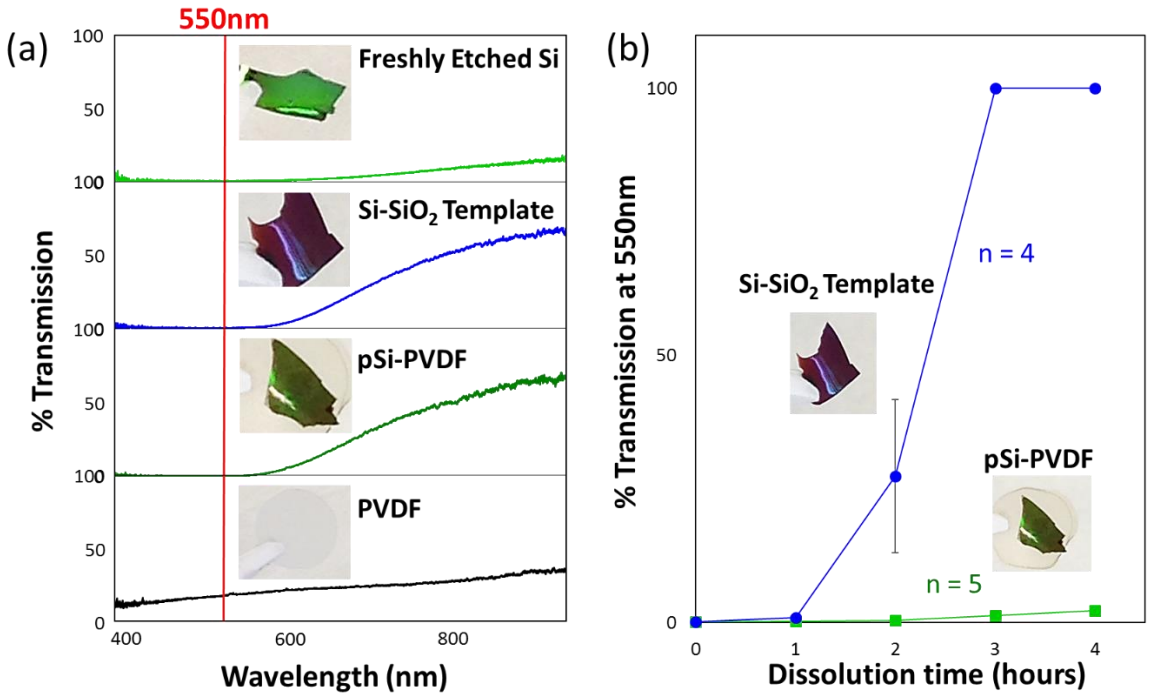

Figure 1.6. (a) Transmission spectra in air with pictures of freshly-etched pSi, the pSi-SiO_2 template, the pSi-PVDF composite before dissolution, and a PVDF disk and (b) Percent transmission at 550nm of the pSi template and the pSi-PVDF composite after 0h, 1h, 2h, 3h and 4h in 0.05M KOH. All data points represent the average of 5 samples for the pSi-PVDF data points and 4 samples for the Si-SiO_2 data points. One of samples for an Si-SiO2 data point was excluded by Dixon's Q-test as an outlier, where a Q-value of 0.765 was used (90% confidence).

1.4 Conclusions

In this chapter, we infiltrated PVDF into a porous silicon rugate structure via the melt-cast method, and then selectively removed the porous silicon template. The resulting sensor exhibited tunable hydrophobicity over a water contact angle range of 60° - 110°, and the dissolution process was slow enough to enable good control over the water contact angle of the surface. The sensor was much more stable in basic conditions than its porous silicon counterpart. We anticipate that this tunable hydrophobicity will present a simple method to enhance the sensitivity of pSi-polymer composite VOC sensors, by tailoring the hydrophobicity of the sensor to the hydrophobicity of the analyte.

Chapter 1, in full, is being prepared for submission for publication of the material. Kennard, Rhiannon; Wang, Joanna; Lee, Gha Y.; Bisiewicz, Rachel H.; Cortez Lemus, Norma A.; Cao, Xiaoyu C.; Anglin, Emily J.; Park, Jennifer S.; Potocny, Andrea; Bernhard, Drew; Li, Jianlin; Sailor, Michael J. The thesis author was the primary investigator and author of this material.

1.5 References

1 King, Brian H., Anne M. Ruminski, Jay L. Snyder, and Michael J. Sailor. "Optical-Fiber-Mounted Porous Silicon Photonic Crystals for Sensing Organic Vapor Breakthrough in Activated Carbon." Advanced Materials 19, no. 24 (2007): 4530-4534.

2 Petrova-Koch, V., Th Muschik, A. Kux, B. K. Meyer, F. Koch, and V. Lehmann. "Rapid-thermal-oxidized porous Si− The superior photoluminescent Si." Applied physics letters 61, no. 8 (1992): 943-945.

3 Ruminski, Anne M., Brian H. King, Jarno Salonen, Jay L. Snyder, and Michael J. Sailor. "Porous Silicon-Based Optical Microsensors for Volatile Organic Analytes: Effect of Surface Chemistry on Stability and Specificity."Advanced Functional Materials 20, no. 17 (2010): 2874-2883.

4 Urmann, Katharina, S. Arshavsky-Graham, Johanna G. Walter, Thomas Scheper, and Ester Segal. "Whole-cell detection of live lactobacillus acidophilus on aptamer-decorated porous silicon biosensors." Analyst (2016).

5 Stewart, M. P., E. G. Robins, T. W. Geders, M. J. Allen, H. Cheul Choi, and J. M. Buriak. "Three methods for stabilization and functionalization of porous silicon surfaces via hydrosilylation and electrografting reactions." *PHYSICA STATUS SOLIDI A APPLIED RESEARCH* 182, no. 1 (2000): 109-116.

6 Vincent, G., Optical properties of porous silicon superlattices. *Appl. Phys. Lett.* 1994, *64* (18), 2367-2369.

7 Bonanno, Lisa M., and Ester Segal. "Nanostructured porous silicon–polymer-based hybrids: from biosensing to drug delivery." *Nanomedicine* 6, no. 10 (2011): 1755-1770.

8 Li, Yang Yang, Frédérique Cunin, Jamie R. Link, Ting Gao, Ronald E. Betts, Sarah H. Reiver, Vicki Chin, Sangeeta N. Bhatia, and Michael J. Sailor. "Polymer replicas of photonic porous silicon for sensing and drug delivery applications." *Science* 299, no. 5615 (2003): 2045-2047.

9 Sailor, Michael J. *Porous silicon in practice: preparation, characterization and applications*. John Wiley & Sons, 2012.

10 Segal, Ester, and Maksym A. Krepker. "Polymer-porous silicon composites." In *Handbook of Porous Silicon*, pp. 187-198. Springer International Publishing, 2014.

11 Kelly, Timothy L., Ting Gao, and Michael J. Sailor. "Carbon and carbon/silicon composites templated in rugate filters for the adsorption and detection of organic vapors." *Advanced Materials* 23, no. 15 (2011): 1776-1781.

12 Wu, Elizabeth C., Jennifer S. Andrew, Lingyun Cheng, William R. Freeman, Lindsey Pearson, and Michael J. Sailor. "Real-time monitoring of sustained drug release using the optical properties of porous silicon photonic crystal particles." *Biomaterials* 32, no. 7 (2011): 1957-1966.

13 Salonen, J., Björkqvist, M., Laine, E. and Niinistö, L., 2004. Stabilization of porous silicon surface by thermal decomposition of acetylene. Applied Surface Science, 225(1), pp.389-394.

14 Wang, Joanna, Jinmyoung Joo, Rhiannon M. Kennard, Sang-Wha Lee, and Michael J. Sailor. "Thermolytic Grafting of Polystyrene to Porous Silicon."Chemistry of Materials 28, no. 1 (2015): 79-89.

15 Jalkanen, T., E. Mäkilä, Y-I. Suzuki, T. Urata, K. Fukami, T. Sakka, J. Salonen, and Y. H. Ogata. "Studies on Chemical Modification of Porous Silicon-Based Graded-Index Optical Microcavities for Improved Stability Under Alkaline Conditions." Advanced Functional Materials 22, no. 18 (2012): 3890-3898.

16 Nallasamy, P., and S. Mohan. "Vibrational spectroscopic characterization of form II poly (vinylidene fluoride)." Indian Journal of Pure and Applied Physics43, no. 11 (2005): 821-827.

17 Ataollahi, N., Azizan Ahmad, Harun Hamzah, Mohd Yusri Abd Rahman, and N. S. Mohamed. "Preparation and characterization of PVDF-HFP/MG49 based polymer blend electrolyte." Int. J. Electrochem. Sci 7, no. 6693 (2012): e6703.

18 Bormashenko, Ye, R. Pogreb, O. Stanevsky, and Ed Bormashenko. "Vibrational spectrum of PVDF and its interpretation." Polymer testing 23, no. 7 (2004): 791-796.

19 Cassie, A. B. D. "Contact angles." Discussions of the Faraday Society 3 (1948): 11-16.

APPENDIX ONE.

SUPPLEMENTARY MATERIALS TO CHAPTER ONE

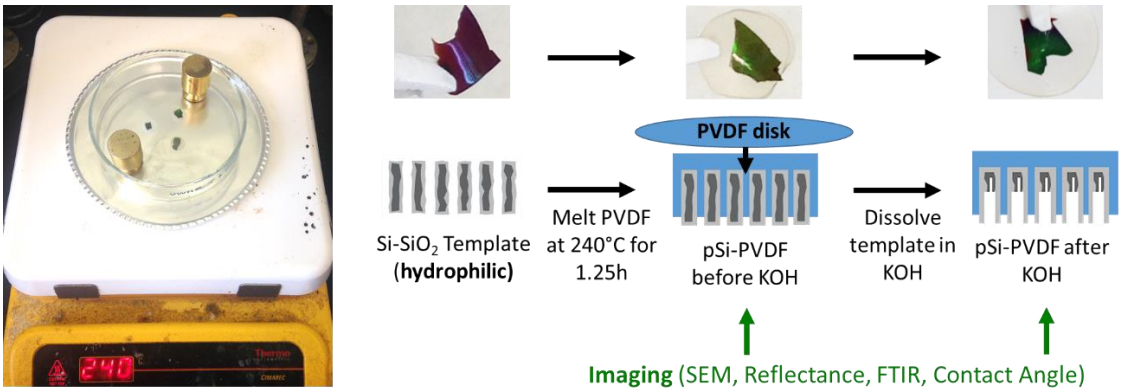

Figure A.1.1. Experimental setup for PVDF infiltration into porous silicon (left) and schematic of PVDF infiltration into porous silicon with pictures of the Si-SiO2 template, pSi-PVDF composite before KOH, and pSi-PVDF composite after KOH (right) taken with IPhone 5c. The samples were imaged on the side opposite to the side on which the PVDF was infiltrated.

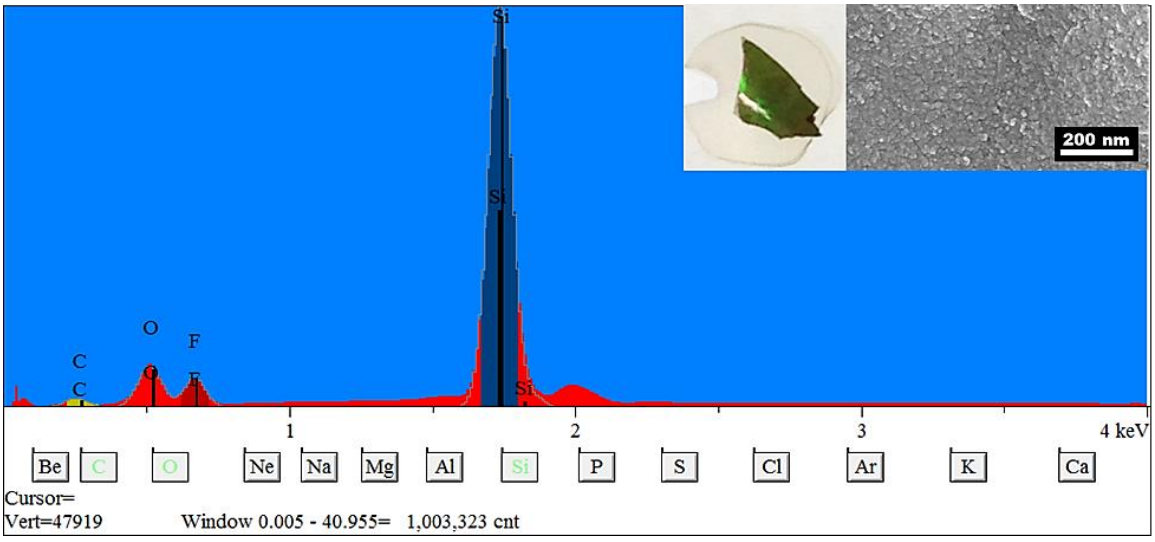

Figure A.1.2. EDX spectrum of a pSi-PVDF composite before dissolution in KOH. Inset are a picture and SEM image of the sample.

The presence of Si, F, O, and C indicate that the area imaged in SEM was indeed the pSi-PVDF composite.

	pSi-PVDF before KOH	pSi-PVDF after 6h in KOH
% weight Si	34	2
% weight F	21	57

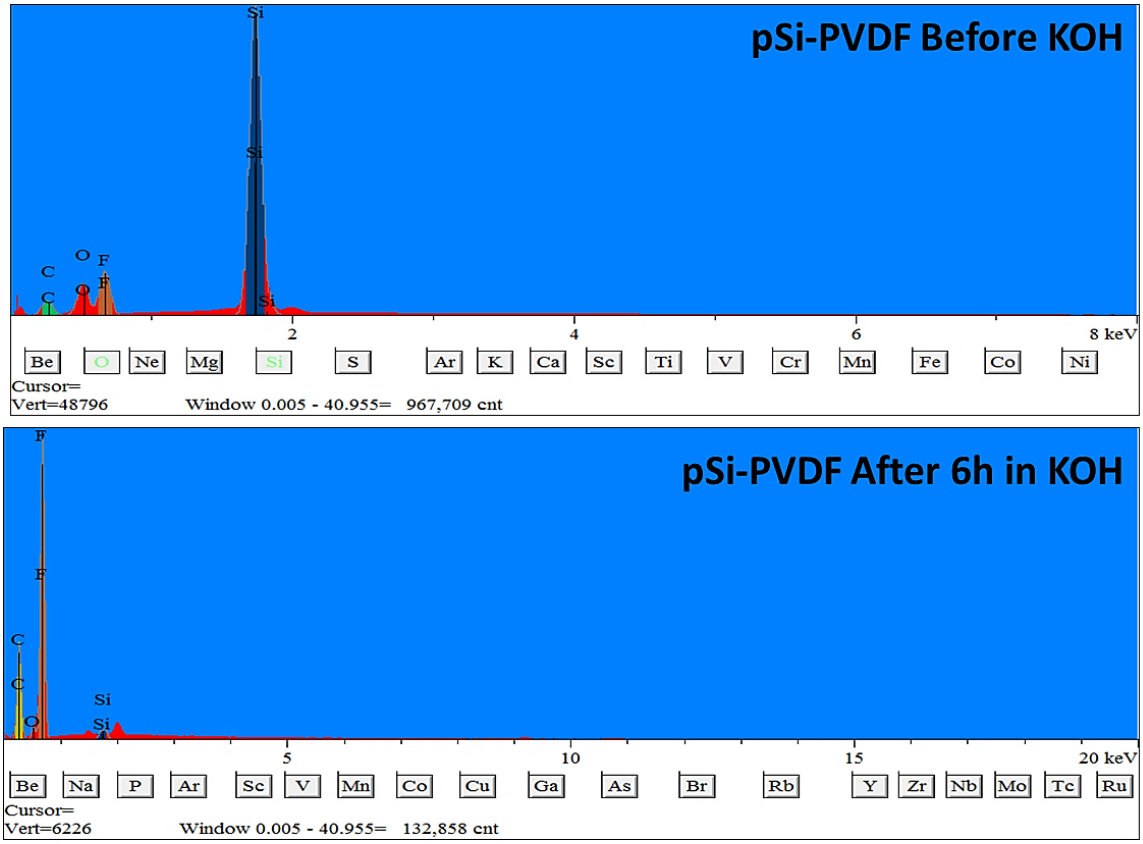

Figure A.1.3. Percent weight Si and F of the composite before KOH and after 6h in KOH (top) and corresponding EDX spectra (middle and bottom).

The decrease in percent weight Si and in the intensities of the Si and O peaks after 6h of soaking time in KOH indicate selective removal of the Si-SiO_2 template.

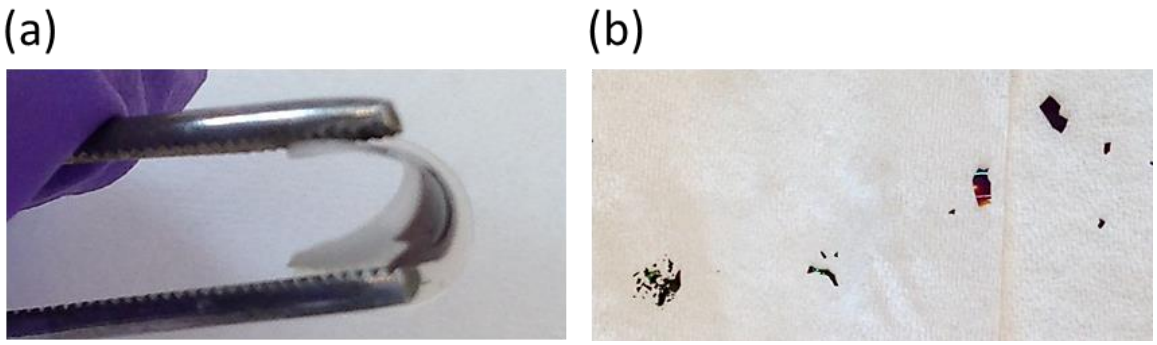

Figure A.1.4. (a) A pSi-PVDF composite is flexed between metal tweezers; (b) the Si-SiO_2 template shatters upon flexing.

CHAPTER TWO.

OPTIMIZATION OF POROUS SILICON MICROPARTICLE SYNTHESIS

2.1 Introduction

Barriers to delivery of ocular therapeutics include the inability of drugs to access the retina via the blood stream and the short half-life of drugs injected into the vitreous. [1] Delivery of ocular therapeutics therefore requires frequent intra-ocular injections, thereby increasing the risk of complications such as infections. These issues put forth the need for a drug delivery system in which a drug carrier releases the therapeutic in a long-term and controlled manner. [1]

Porous silicon microparticles have been investigated as ocular therapeutic delivery agents due to their biocompatibility in vivo and particularly in the vitreous, to their high payload capacity, and to their ability to retain the drug's activity during delivery in vivo. [1] Key parameters controlling drug release rates include particle size and particle functionalization. Particles with sizes in the range of 10 to several hundred microns have large payload capacities and in vivo residence times on the scale of months. [1] The slow dissolution of these particles allows gradual release of the therapeutic directly into the vitreous. Surface functionalizations such as the formation of a stable SiO_2 layer on the surface of the particles or thermal carbonization have been shown to slow particle dissolution rate. [1, 2]

Efficient production of uniform porous silicon microparticles is thus of interest for delivery of ocular therapeutics. Salonen and others have developed electrochemical perforation etching as a means to improve particle yield and size distribution. [2, 3] By alternating the desired current density with high-current density pulses, thin, high-porosity regions are generated in the porous layer that act as artificial cleavage planes along which the layer preferentially breaks during ultrasonication. While certain conditions have been

systematically investigated for nanoparticle synthesis using perforated etching, a systematic investigation of conditions has not been performed for microparticle synthesis. [3] In particular, no study has investigated which ultrasonication conditions are necessary to maximize maximum microparticle yield. In the ultrasonication baths commonly used in porous silicon synthesis, sound waves travel through a water bath and through the solvent in which the films are contained. [4] The high and low amplitude points of the sound waves cause dissolved gas in the liquid to expand (void/bubble formation), then violently contract (cavitation), releasing much heat and compressing the material surrounding the bubble. [5] This violent compression results in fracture of porous silicon films surrounding the bubble. Rough surfaces are known to facilitate bubble formation (bubble nucleation), either by releasing trace amounts of gas adsorbed on the surface or by providing sites where gases dissolved in the liquid can form a bubble. [5, 6] Porous silicon has a very rough surface, so the rate and uniformity of bubble nucleation on the silicon surface may greatly impact the efficiency of ultrasonication.

In this work, we investigated some of the perforated etching conditions most likely to affect microparticle synthesis, focusing on the ultrasonication step. We investigated the impact of the amount of cavitation on particle size and size distribution after ultrasonication. We then optimized silicon concentration during ultrasonication and the duration of ultrasonication for synthesis of ~70µm-sized particles with low size distribution. We hypothesized that bubble nucleation and cavitation may not occur uniformly in thick porous silicon films. We therefore introduced a pre-sonication crushing step, and evaluated the impact of the uniformity of cavitation/nucleation within porous silicon films on particle yield.

2.2 Experimental Section

2.2.1 Materials

Silicon wafers, highly boron-doped (resistivity < 0.0015 Ω-cm), polished on the (100) face, 525 ± 25 μm thick were purchased from Virginia Semiconductors.

2.2.2 Etching of Porous Silicon and Mechanical Crushing of Free-Standing Films

Porous silicon microparticles were synthesized by electrochemical etching of p-type (100) crystalline silicon wafers (0.0009-0.0010 Ohm.cm,) using a solution of 1:1 HF (48% aqueous): ethanol by volume (CAUTION: HF is highly toxic and fumes and contact with skin should be avoided), following published procedures. [2, 4] A polyether ether ketone AMMT Single5 525 micron (S-100-EC-611311) etching system was used with a platinum meche as the counter electrode and graphoil as the working electrode. A 50mA/cm^2 current density was applied for 40 min, followed by a high-density current pulse (167mA/cm^2) to introduce a perforation layer (Fig. 2.1b), and a zero-current period to allow diffusional recovery of the electrolyte concentration. [2] Three 50mA/cm^2 layers were etched (Fig. 2.1a). We refer to the 50mA/cm^2 layers as primary layers and the 167mA/cm^2 layers as perforation layers. A single 50mA/cm^2 layer was etched separately for comparison. Etching waveforms were generated in a computer program written in Labview (National Instruments, Inc.) and the etch was driven by a Keithley 2651A High Power Source Meter power supply interfaced to the Labview program. For all etches, porosity and thickness were calculated using the SLIM technique, with ethanol as the filling liquid, pSi skeleton refractive index of 2.1, and using a CCD spectrometer (Ocean Optics USB-4000) fitted to a bifurcated fiber optic cable with a tungsten light source (Ocean Optics LS-1). [4]

All films were lifted off from the silicon wafer using a current density of 20mA/cm^2 for 8 min using a 1:29 HF:Ethanol solution. The free-standing, partially fragmented (cm-scale) films were dried in a vacuum oven for 5h and weighed for the ultrasonication studies (typically 3-30mg of film). A portion of the films was then mechanically fractured by crushing in ethanol to approximately 1mm. The crushing apparatus used was a glass vial and a glass rod. All films were stored in ethanol.

2.2.3 Ultrasonication of Porous Silicon Films

For size and size distribution optimization experiments, the crushed films were sonicated in 4mL glass vials in a constant volume of 1.5mL, in concentrations ranging from 2-20mg/mL (3-30mg of particles weighed out) using an Ultrasonic Cleaner (VWR Symphony Model 97043-932, Operating Frequency 35kHz, RF-Power 48W). Care was taken to always sonicate the samples in the same location in the sonicator, and to keep the temperature between 20°C and 30°C. Sonication time varied from 5min to 60min (Fig. 2.2). The single layers and non-crushed layers were also sonicated in 4mL vials in 1.5mL ethanol. For some samples, the volume was varied between 0.5mL and 3mL (Fig. 2.2). Nanoparticles and small microparticles (<10μm) were removed by letting the particles settle for 30 seconds and exchanging the supernatant. This rinsing procedure was repeated 3 times.

2.2.4 Imaging and Particle Size and Size Distribution Analyses

The approach for calculating size and size distribution is outlined in Figure 2.1. Films and particles were imaged using a Scanning Electron Microscope (SEM - FEI XL30 with accelerating voltage of 7kV and spot size of 3 nm) and Nikon CoolPix 4300 camera fitted to an optical microscope. For SEM, the samples were first sputter-coated with iridium

(Emitech K575X Sputter Coater). Average particle size and size distribution were obtained by analyzing the optical microscope images using Image J (National Institutes of Health) and OriginPro software. For Image J analysis, the optical microscope images were taken at 5x magnification and 30 images were used per sample. Size distribution was calculated as the standard deviation of the particle sizes. Both average particle size and size distribution were calculated for particles smaller than 300μm, in order to minimize the contribution of large outlier particles. The number of particles above 300μm in size was recorded separately for each sample. SEM images and Image J software was also used to determine pore size for the primary and perforation layers.

2.2.5 Calculation of Yield

Yield was calculated as the percent weight of particles recovered from the films after ultrasonication, rinsing, and removal of particles larger than 300μm:

$$\% \text{ Yield} = 100 \text{ x } \frac{\text{Weight of particles after rinsing and filtering}}{\text{Weight of film before ultrasonication}} \quad (1)$$

Removal of particles larger than 300μm was accomplished by filtering the ultrasonicated samples using a 23-gauge needle (i.d. = 337μm) and a plastic syringe.

2.3 Results and Discussion

2.3.1 Synthesis of Perforated Etched Films and Microparticles

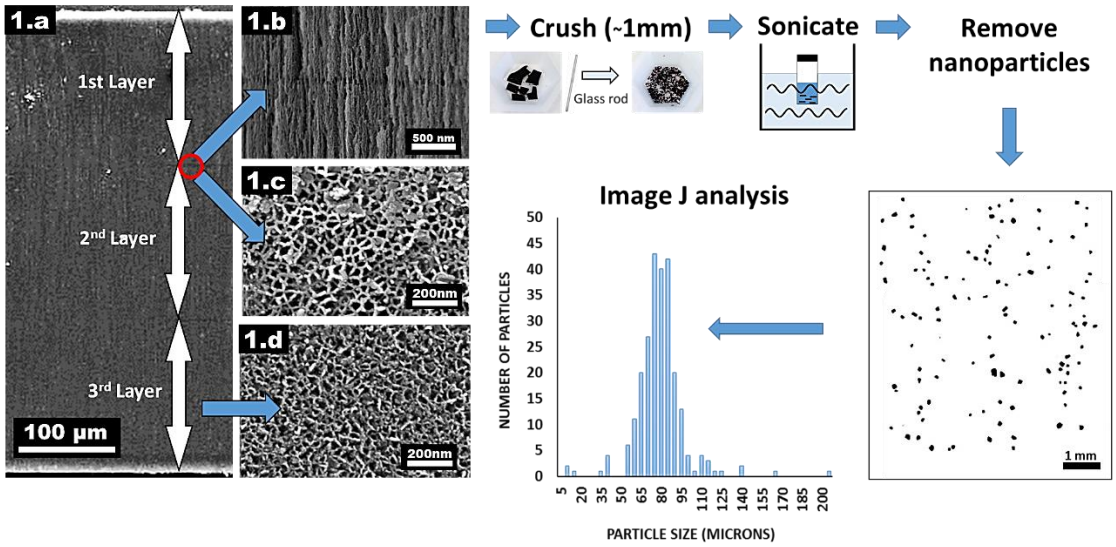

Figure 2.1. Approach used for size and size distribution analysis. SEM images of (a) cross-section of a film with three primary layers and two perforation layers, (b) zoom on a perforation layer, (c), top view of a perforation layer and (d) top view of a primary layer.

The approach used to prepare microparticles is outlined in Figure 2.1. Three primary layers were etched; separated by two perforation layers. SEM images of the perforated-etched film revealed primary layers of ~70µm thickness and ~20nm pore size (Fig. 2.1a and 2.1d) and perforation layers of ~60nm thickness and ~40nm pore size (Fig. 2.1b and 2.1c). The SEM thicknesses were used to calculate porosity of the primary and perforation layers using the SLIM technique, with ethanol as the filling liquid. [4] The porosity of the primary layer was ~50%, and that of the perforation layer was ~80%.

2.3.2 Effect of Increasing the Number of Cavitation Sites on Ultrasonication Efficiency

The number of cavitation sites was increased by increasing the volume of solvent (ethanol), while keeping the mass of silicon (number of nucleation sites) constant (Fig. 2.2). All samples were ultrasonicated for 5min. At low volume, large chunks remained in

the sample. As the volume was doubled, then tripled, the particle size decreased, and the particle size distribution seemed to be decently uniform (Fig. 2.2). Increasing the number of cavitation sites (volume of solvent) therefore increased the efficiency of ultrasonication.

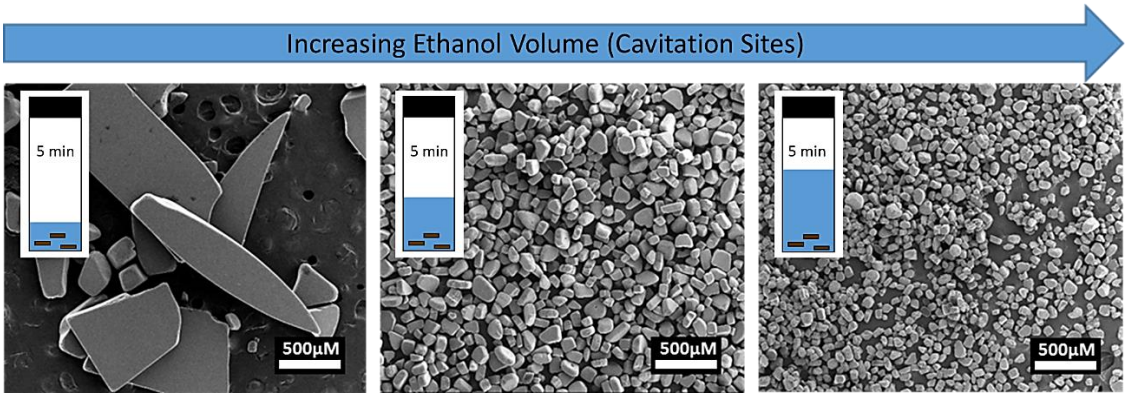

Figure 2.2. SEM images of 9mg perforated layers sonicated for 10min in (a) 0.45mL ethanol, (b) 1.5mL ethanol, and (c) 3mL ethanol.

We then performed a systematic study of this effect, to investigate it more thoroughly and to render the results of this study applicable to experiments in which the ultrasonicator used has different power or frequency output than our ultrasonicator (Fig. 2.3). Specifically, we kept the volume of ethanol (number of cavitation sites) constant, and we decreased the mass of Si per vial, so that the number of cavitation sites would increase relative to the number of nucleation sites. Several different ultrasonication durations were tested (Fig. 2.3). Average particle size, particle size distribution, and the number of particles larger than 300µm (large chunks) were calculated for all samples (Fig. 2.3). The average size and size distribution were calculated for particles smaller than 300µm, so that the results would not be influenced by outlier values. Size distribution was calculated to be the standard deviation of the average particle size, using a Gaussian distribution.

Average particle size, size distribution and the number of particles >300µm increased with the mass of Si for all ultrasonication times (Fig. 2.3, black arrows). This

confirms that increasing the number of cavitation sites relative to the number of nucleation sites increases ultrasonication efficiency.

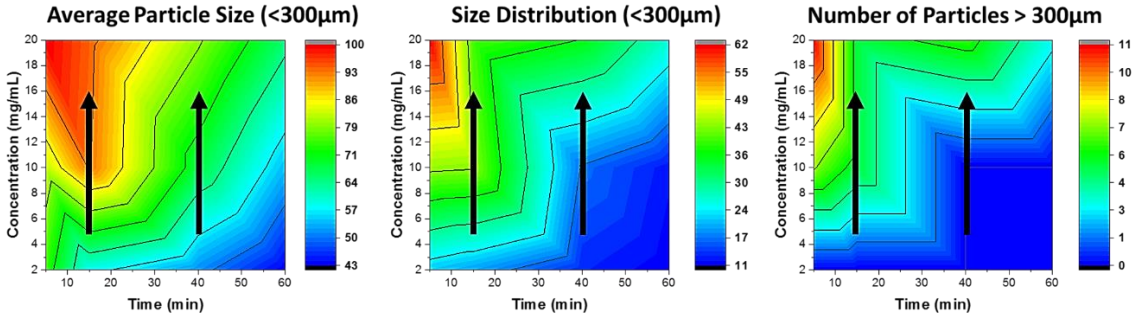

Figure 2.3. Contour charts of the average particle size and size distribution for particles < 300µm, and the number of particles > 300µm in each sample. The size distribution was calculated as the standard deviation of the particle size. All data points are the average of 3 measurements.

2.3.3 Optimization of Ultrasonication Concentration and Time for Synthesis of ~70µm Particles

We used the results from the above study (Fig. 2.3) to optimize ultrasonication concentration and time for synthesis of ~70µm particles (white line in Fig. 2.4a) with low size distribution (blue area below the black line in Fig. 2.4b) and low number of particles >300µm (blue area below the black line Fig. 2.4c). We then combined the requirements for size, size distribution, and number of particles >300µm (Fig. 2.4d). Two optimal ultrasonication conditions were found (red circles in Fig. 2.4d): 2mg/mL for 5min and 10mg/mL for 40min. 2mg/mL for 5min (red dotted circle in Fig. 2.4d) presented the advantage of very low ultrasonication time. However, the number of particles ultrasonicated was very low (2mg), so this condition was not very efficient and wasted solvent. The 10mg/mL for 40min condition (red solid circle in Fig. 2.4d) was less wasteful of solvent and ultrasonicated the particles in an acceptable amount of time (40min), so 10mg/mL for 40min was considered the optimal condition.

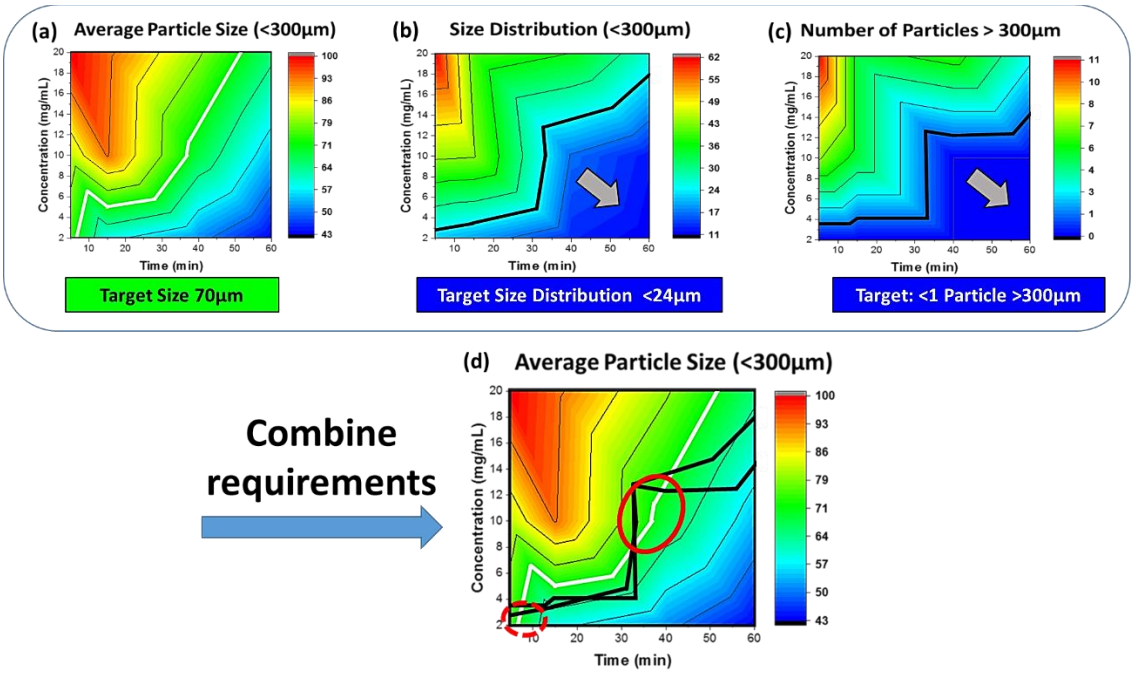

Figure 2.4. Contour charts of the (a) average particle size and (b) size distribution for particles < 300µm, (c) the number of particles > 300µm in each sample, and (d) combination of requirements for optimized ultrasonication conditions (solid red circle). The white line in (a) represents the target particle size (~70µm); the black lines in (b) and (c) represent the maximum acceptable size distribution and number of particles >300µm. Gray arrows are drawn for emphasis. The red circles in (d) represent the conditions in which conditions (a-c) are met, the solid red circle represents the condition that does not waste solvent.

2.3.4 Introduction of a Pre-Ultrasonication Crushing Step

To investigate the importance of uniformity of nucleation sites during the ultrasonication procedure, we compared the yield of ~70µm particles from samples in which the films were or were not crushed before ultrasonication (Fig. 2.5). We chose crushing before ultrasonication as a means to test uniformity because we hypothesized that smaller films may have greater nucleation uniformity than larger films.

Crushing the films to ~1mm in size before ultrasonication was found to significantly improve ultrasonication yield of ~70µm particles (Fig. 2.5b). SEM pictures revealed that samples ultrasonicated without crushing contained a mix of large chunks and smaller particles (Fig. 2.5a). The large chunks seemed to break preferentially at the perforation layer sites, but also at the exterior edges of the chunks, presumably because the

chunks were large enough to mask the intensity of the sound waves and thus decrease rate of nucleation at the center of the chunks. Samples ultrasonicated with the crushing step exhibited much more uniformly-sized particles (Fig. 2.5a), and correspondingly much higher yield of ~70μm particles (Fig. 2.5b). The percent yield was also more reproducible for samples with crushing than it was for samples without crushing, as evidenced by the much lower uncertainty in the yield of samples with crushing (Fig. 2.5b).

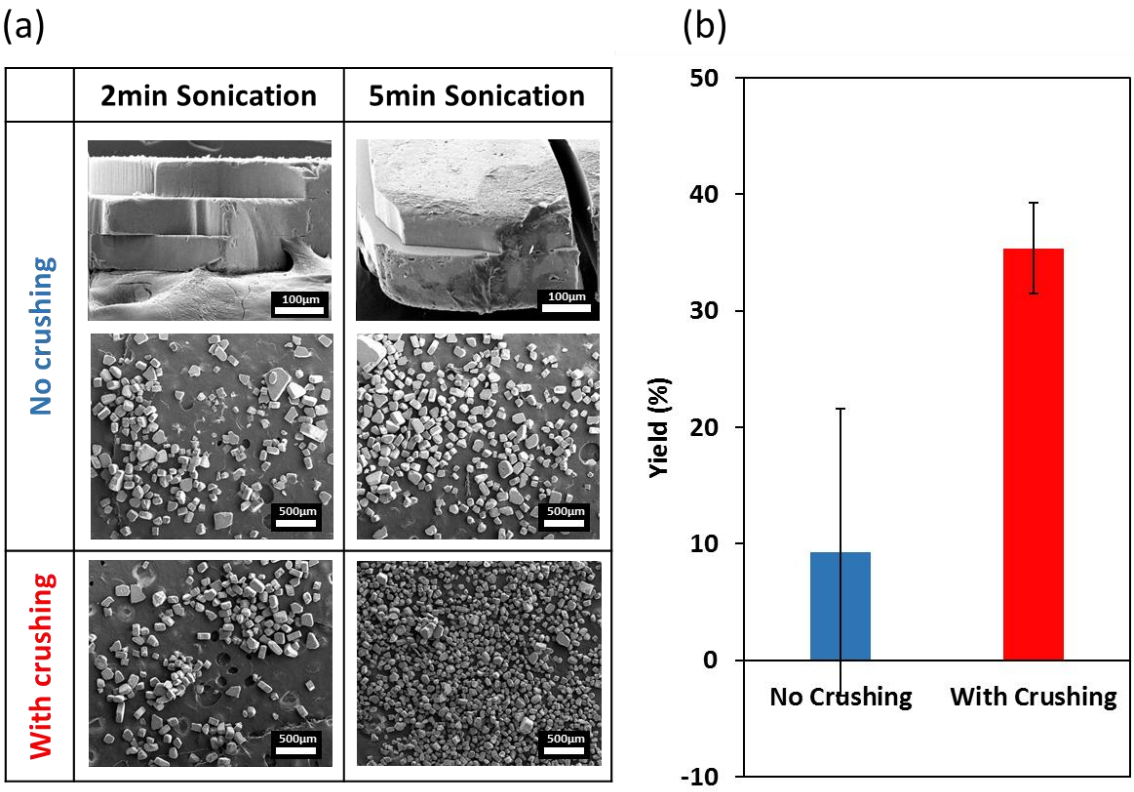

Figure 2.5. (a) SEM images of 2mg/mL perforated layers sonicated with and without pre-ultrasonication crushing for 2 and 5 min. (b) Yield of microparticles with and without crushing ultrasonicated at 10mg/mL for 40min after filtration.

2.4 Conclusions

Potential factors affecting the yield of microparticles synthesized using the perforated etching method were investigated. We focused our attention on the ultrasonication step, specifically on the effects of increasing the amount of cavitation and of increasing nucleation uniformity. Increasing cavitation relative to nucleation was found to yield smaller size distribution. We then optimized porous silicon particle concentration during ultrasonication and duration of ultrasonication for synthesis of ~70μm particles. Crushing the silicon films before ultrasonication was found to significantly increase and improve reproducibility of particle yield, presumably because the density of nucleation sites in smaller films was more uniform. We anticipate that our systematic investigation may be applied to studies in which the ultrasonicator used has different power output than the ultrasonicator used in this study.

Chapter 2, in full, is being prepared for submission for publication of the material. Kennard, Rhiannon; Sailor, Michael J. The thesis author was the primary investigator and author of this material.

2.5 References

1 Hou, H., Nieto, A., Ma, F., Freeman, W. R., Sailor, M. J., & Cheng, L. (2014). Tunable sustained intravitreal drug delivery system for daunorubicin using oxidized porous silicon. Journal of Controlled Release, 178, 4654.

2 Bimbo, L. M., Sarparanta, M., Santos, H. A., Airaksinen, A. J., Mäkilä, E., Laaksonen, T., & Salonen, J. (2010). Biocompatibility of thermally hydrocarbonized porous silicon nanoparticles and their biodistribution in rats. ACS nano, 4(6), 3023-3032.

3 Qin, Z., Joo, J., Gu, L., & Sailor, M. J. (2014). Size control of porous silicon nanoparticles by electrochemical perforation etching. Particle & Particle Systems Characterization, 31(2), 252-256.

4 Sailor, Michael J. *Porous silicon in practice: preparation, characterization and applications*. John Wiley & Sons, 2012.

5 Kentish, Sandra, and Muthupandian Ashokkumar. "The physical and chemical effects of ultrasound." In Ultrasound technologies for food and bioprocessing, pp. 1-12. Springer New York, 2011.

6 Sliwa, John, and Carol Tosaya. "Apparatus and method for delivering acoustic energy through a liquid stream to a target object for disruptive surface cleaning or treating effects." U.S. Patent Application 11/729,567, filed March 28, 2007.

APPENDIX TWO.

SUPPLEMENTARY MATERIALS TO CHAPTER TWO

A.2.1 Average Particle Size, Size Distribution, and Number of Particles>300µm with Respective Uncertainties.

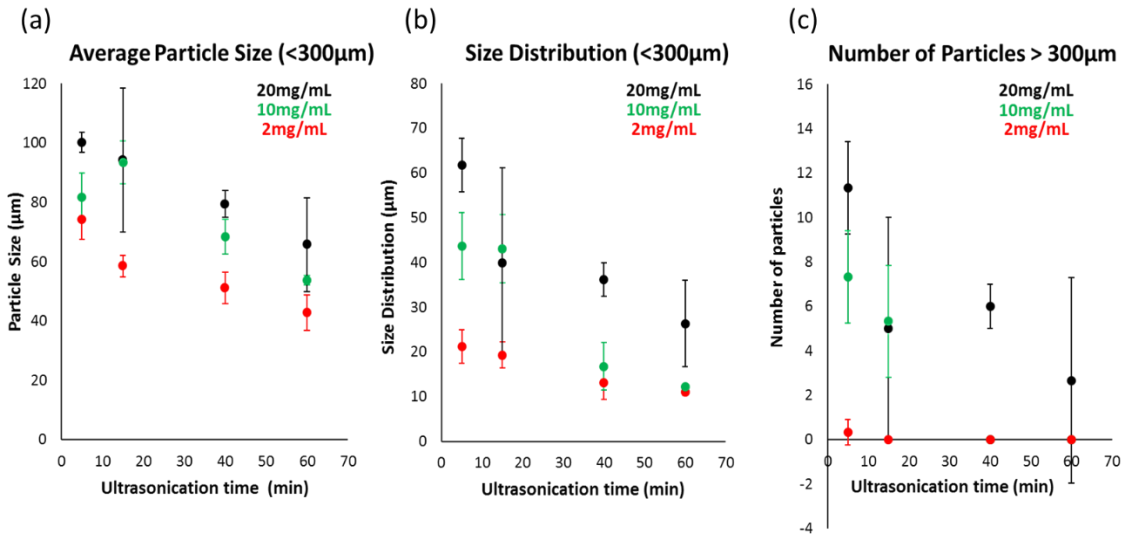

Figure A.2.1. Graphs of (a) the average particle size and (b) size distribution for particles < 300µm, and (c) the number of particles > 300µm in each sample. The size distribution was calculated as the standard deviation of the particle size. All data points are the average of 3 measurements.

The uncertainties for the 2mg/mL samples were consistently small, indicating good reproducibility, and consistent with the interpretation that higher cavitation density increased the efficiency of ultrasonication. Correspondingly, the uncertainties for the 20mg/mL samples were large, indicating lower reproducibility.

The 10mg/mL sample ultrasonicated for 40min had low uncertainties in the average size, size distribution, number of particles larger than 300µm, indicating good reproducibility. The 40min and 60min data points for the 10mg/mL samples are not visible in Figure A.2.1c because they overlap with the data points for the 2mg/mL samples.

A.2.2 Comparison with Ultrasonication of Non-Perforated Layers

We investigated the differences between ultrasonicating perforated vs. non-perforated layers (Fig. A.2.2). To do so, we sonicated perforated and non-perforated layers for 5 minutes (Fig. A.2.2), and compared average particle size (<300µm), particle size

distribution (<300μm), and the number of particles larger than 300μm. Perforated layers sonicated at the same concentration as non-perforated layers exhibited similar average particle size, but larger size distribution and much larger number of particles >300μm (Fig. A.2.2), presumably because the local silicon density in the perforated layers was greater, so the nucleation density would be lower. It was thus necessary to sonicate perforated layers at lower concentrations than non-perforated layers at the 10mg/mL concentration (Fig. A.2.2). However, more work is required before concluding whether perforated or non-perforated etching is more efficient for microparticle synthesis.

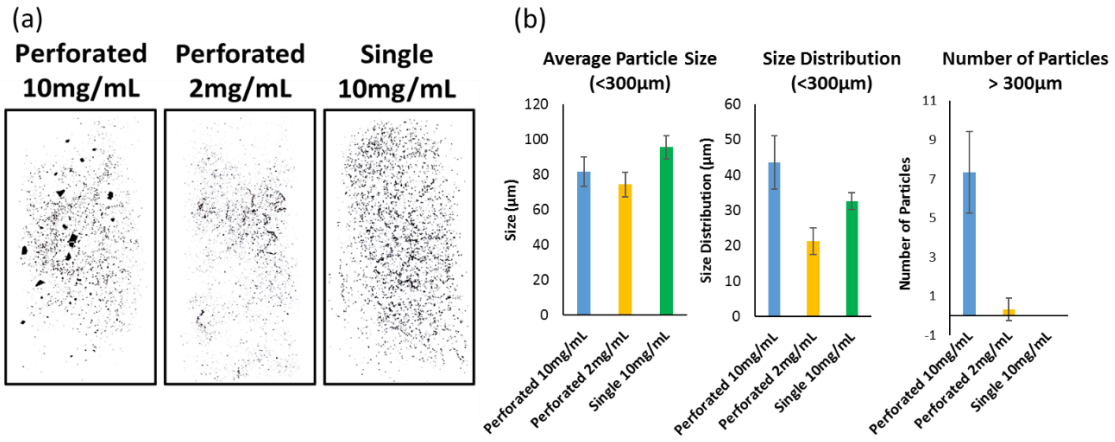

Figure A.2.2. (a) Photographs of particles on microscope slides and (b) average particle size (<300μm), size distribution (<300μm), and number of particles >300μm; for perforated-etched samples ultrasonicated at 10mg/mL and 2mg/mL and single layer-etched ultrasonicated at 10mg/mL, all ultrasonicated for 5min.